

DNS OF COMPRESSIBLE TURBULENT FLOW IN CONVERGENT-DIVERGENT NOZZLES WITH ISOTHERMAL WALLS

Susila Mahapatra, Somnath Ghosh
Department of Aerospace Engineering,
Indian Institute of Technology, Kharagpur, India

INTRODUCTION

Compressible wall-bounded turbulent flows occur in high-speed flight. Development of accurate Reynolds stress models for compressible shear flows still remains a challenging task, particularly the modelling of pressure-strain correlations. DNS of supersonic channel flows with isothermal walls (Coleman *et al.*, 1995; Foysi *et al.*, 2004) have revealed that compressibility effects are associated with mean density and temperature variations in the near-wall region. The reduction of pressure-strain correlations at supersonic Mach numbers leads to an increase in Reynolds stress anisotropy (Foysi *et al.*, 2004). Similar effects were also observed in DNS of supersonic pipe flow with isothermal wall (Ghosh *et al.*, 2010). Effects of mean dilatation and extra rates of strain lead to changes in the turbulence structure in supersonic wall-bounded flows which cannot be explained by mean property variations only. These effects were described by Bradshaw (1974) and observed in LES and DNS of canonical supersonic nozzle and diffuser flows where fully developed supersonic pipe flow was used as inflow (Ghosh *et al.*, 2008; Ghosh & Friedrich, 2014). It was observed that the Reynolds stresses decrease in the nozzle and increase in the diffuser. The pressure-strain correlations play an important role in changing the Reynolds stresses in these flows. In the present study, we perform DNS of flow through convergent-divergent nozzles with subsonic, turbulent pipe flow as inflow condition. The nozzles investigated here are with and without bell-shaped divergent portions. The objective is to study the changes in turbulence structure in detail as the flow undergoes transition from subsonic to supersonic state in these nozzles.

MATHEMATICAL AND COMPUTATIONAL DETAILS

The governing equations for compressible flow written in generalized curvilinear coordinates in a characteristic form (Sesterhenn, 2001) involving the primitive variables pressure, velocity and entropy are solved using the 5th order low-dissipation compact upwind finite difference scheme of Adams & Shariff (1996) to discretise the convective terms and 6th order compact central scheme of Lele (1992) to compute the viscous and heat flux terms. Time integration is carried out using a low-storage 3rd order Runge-Kutta scheme (Williamson, 1980). These schemes have also been used to study supersonic flow through pipe, nozzle and diffuser by means of DNS (Ghosh *et al.*, 2010; Ghosh & Friedrich, 2014). The flow configuration studied here consists of convergent-divergent (C-D) nozzles with and without bell-shaped divergent portions where inflow conditions

are from fully-developed subsonic turbulent pipe flow having centerline Mach number of 0.37 and friction Reynolds number of 214. The incoming pipe flow is from a separate simulation using streamwise periodic boundary conditions. The pipe flow and nozzle flow simulations are run simultaneously and are coupled using MPI routines and the concept of characteristics. The pipe and nozzle (diffuser) flow domains are each of size $10R \times 2\pi R \times R$ in axial (x), circumferential (θ) and radial (r) directions and are discretized using $256 \times 128 \times 91$ points. The walls of the pipe and the nozzle are isothermal and are kept at the same temperature, $T_w = 276K$. Partially non-reflecting outflow conditions, based on characteristics following Poinot & Lele (1992), are prescribed for the nozzles. The area distribution of the nozzle without bell-shape (case 1) is specified using isentropic streamtube equations as described in Ghosh *et al.* (2008), while method of characteristics is used to generate the area distribution for the bell-shaped nozzle (case 2).

RESULTS

We first present instantaneous azimuthal velocity fluctuations in an axial-radial plane in the nozzles in figures 1 and 2. We notice a general elongation of the near-wall streamwise “streaky” structures as the flow proceeds along the nozzles. Although the turbulent activity is seemingly reduced, relaminarization does not occur as seen in the plots. Figure 3 shows the axial variation of mean centerline and wall pressure along the nozzles and we note that there is a large region of nearly constant negative pressure gradient in nozzle 1. For nozzle 2 the region of constant negative pressure gradient is smaller and there is a pressure recovery in the bell-shaped region after about $x/L = 0.7$. Figure 4 shows the radial Mach number profiles along the two nozzles and we note the near-sonic conditions in the throat regions ($x/L = 0.6$ for case 1 and $x/L = 0.5$ for case 2). The flow downstream of the throat accelerates to supersonic states in the nozzles. However, the effects of the different geometries on the Mach number profiles in the divergent portion is evident, namely there is deceleration in the near-wall region in the bell-shaped nozzle at $x/L = 0.8$. Due to the constant temperature wall and due to cooling of the flow on account of expansion in the nozzles, we note that the core temperature is lower in the nozzles than the wall temperature as the flow becomes supersonic (fig. 5). We also note that in the near-wall region for case 2, a smaller temperature gradient is seen at $x/L = 0.8$ compared to $x/L = 0.5$. This is attributed to a weak compression occurring due to the bell-shaped divergent portion, the effects of which also appear in the Reynolds stress profiles. The mean density is

approximately inversely proportional to the mean temperature in these flows and this is evident in the radial mean density profiles (fig. 6).

We show the normal Reynolds stresses and the Reynolds shear stress profiles in the nozzles, normalized with the local wall shear stress in figures 7-10 where we note attenuation of turbulence due to flow expansion and acceleration. We also note that for case 2, there is a small increase in the near-wall peak of axial Reynolds stress at $x/L = 0.8$ from its value at $x/L = 0.5$ due to the weak compression in the bell-shaped divergent portion. However such a trend is not observed in the azimuthal and radial stresses. The Reynolds shear stress shows a negative peak close to the wall at $x/L = 0.25$ in both nozzles. The larger near-wall peak in the shear stress at $x/L = 0.8$ is again observed similar to the axial stress.

The production, dissipation and pressure-strain correlation terms (normalized with local wall shear stress and viscosity) of the axial Reynolds stress transport equation is shown at two different axial locations along the nozzles in figures 11-12. At $x/L = 0.25$ (in the converging section), we note that the production becomes negative away from the near-wall region in both nozzles. In the divergent portion at $x/L = 0.8$ (fig.12), all the terms are smaller compared to their upstream values. Distinct differences in the magnitude and behaviour of these terms in the two nozzles are noted.

1 Conclusions

DNS of compressible flow through convergent-divergent nozzles with isothermal walls is performed. The nozzle are with and without bell-shaped diverging portions. A decrease in pressure, temperature, density as well as a decrease in Reynolds stresses is observed along the nozzles. A local increase in axial Reynolds stress and the Reynolds shear stress is observed in the bell-shaped diverging portion of the nozzle 2 due to local flow compression.

The authors acknowledge the support of Science and

Engineering Research Board (SERB), DST, India towards this work.

REFERENCES

- Adams, N. A. & Shariff, K. 1996 A high-resolution hybrid compact-ENO scheme for shock-turbulence interaction problems. *Journal of Computational Physics* **127**, 27–51.
- Bradshaw, P. 1974 The effect of mean compression or dilatation on the turbulence structure of supersonic boundary layers. *Journal of Fluid Mechanics* **63**, 449–464.
- Coleman, G. N., Kim, J. & Moser, R. D. 1995 A numerical study of turbulent supersonic isothermal-wall channel flow. *Journal of Fluid Mechanics* **305**, 159–183.
- Foysi, H., Sarkar, S. & Friedrich, R. 2004 Compressibility effects and turbulence scalings in supersonic channel flow. *Journal of Fluid Mechanics* **509**, 207–216.
- Ghosh, S., Foysi, H. & Friedrich, R. 2010 Compressible turbulent channel and pipe flow: similarities and differences. *Journal of Fluid Mechanics* **648**, 155–181.
- Ghosh, Somnath & Friedrich, Rainer 2014 Effects of distributed pressure gradients on the pressure-strain correlations in a supersonic nozzle and diffuser. *Journal of Fluid Mechanics* **742**, 466–494.
- Ghosh, S., Sesterhenn, J. & Friedrich, R. 2008 Large-eddy simulation of supersonic turbulent flow in axisymmetric nozzles and diffusers. *International J. of Heat and Fluid Flow* **29**, 579–590.
- Lele, S.K. 1992 Compact finite difference schemes with spectral-like resolution. *Journal of Computational Physics* **103**, 16–42.
- Poinsot, T. J. & Lele, S. K. 1992 Boundary conditions for direct simulations of compressible viscous flows. *Journal of Computational Physics* **101**, 104–129.
- Sesterhenn, J. 2001 A characteristic-type formulation of the Navier-Stokes equations for high order upwind schemes. *Computers and Fluids* **30**, 37–67.
- Williamson, J. K. 1980 Low-storage Runge-Kutta schemes. *Journal of Computational Physics* **35**, 48–56.

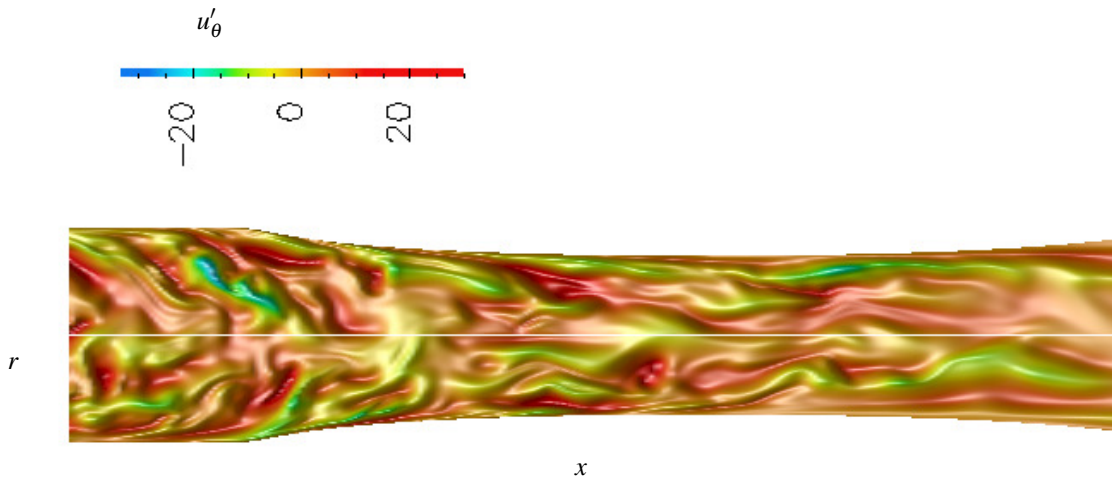


Figure 1. Azimuthal velocity fluctuations in an axial-radial ($x-r$) plane in the C-D nozzle, case 1.

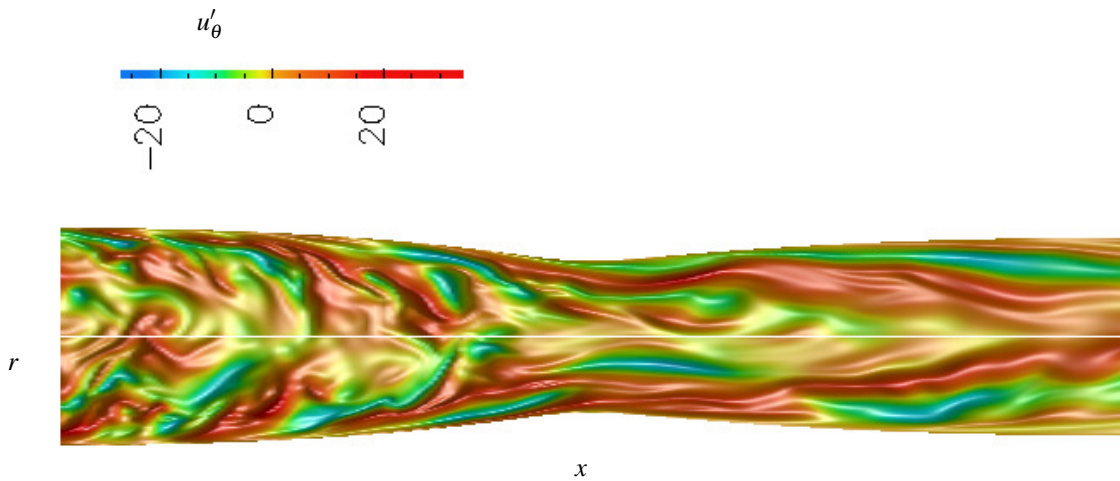


Figure 2. Azimuthal velocity fluctuations in an axial-radial ($x-r$) plane in the C-D nozzle, case 2

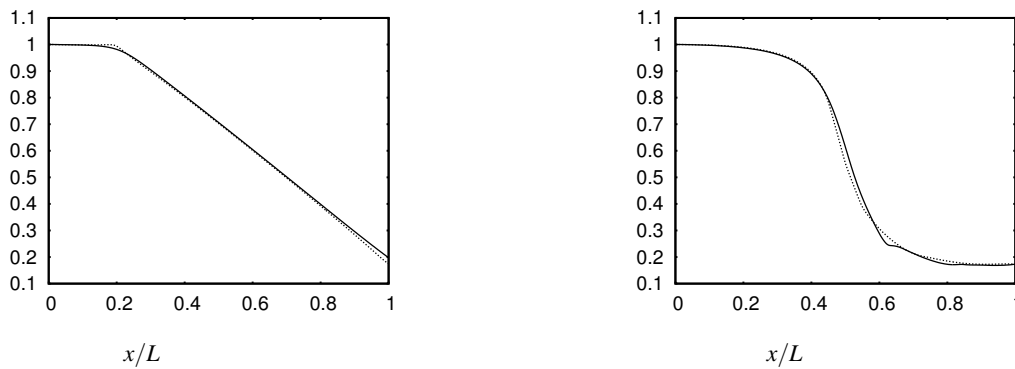


Figure 3. Centerline (solid line) and wall pressure (dashed line), normalized with their inlet values, along the nozzle for case 1(left) and case 2 (right).

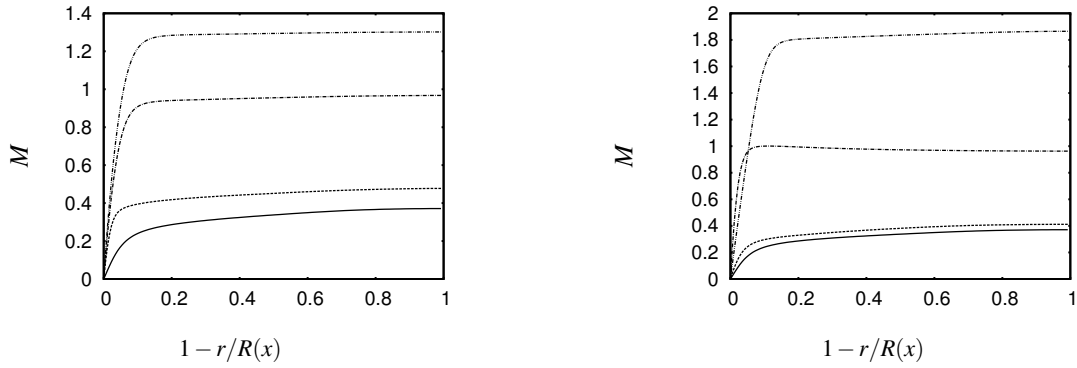


Figure 4. Mean Mach number profiles for case 1(left) and case 2 (right) at — $x/L = 0$, ... $x/L = 0.25$, -.-.- $x/L = 0.6$ (left figure), $x/L = 0.5$ (right figure) and ... $x/L = 0.8$.

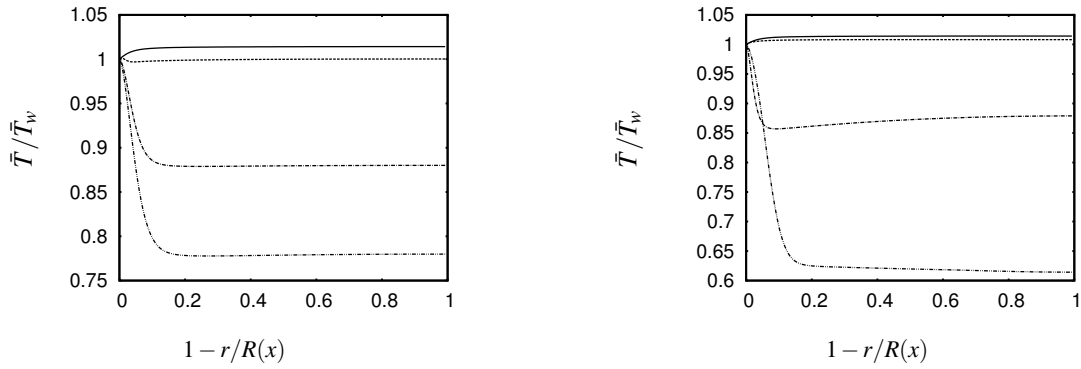


Figure 5. Mean temperature profiles for case 1 (left) and case 2 (right). Line types as in figure 4

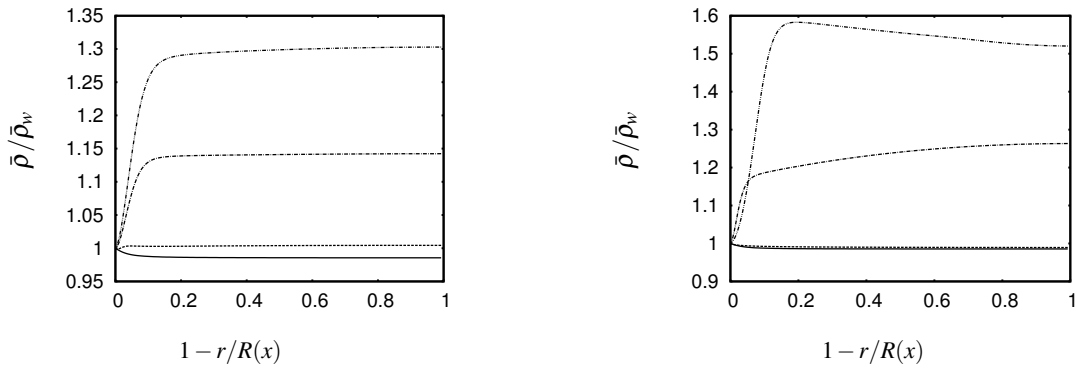


Figure 6. Mean density profiles for case 1 (left) and case 2 (right). Line types as in figure 4

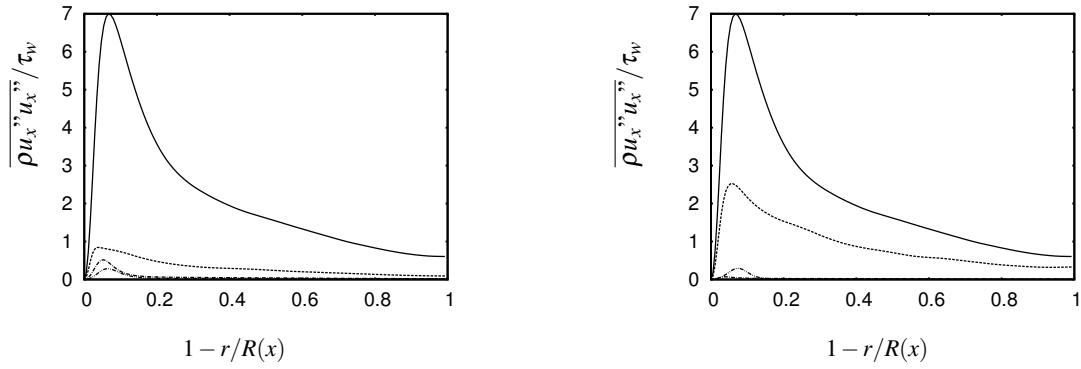


Figure 7. Axial Reynolds stress profiles for case 1 (left) and case 2 (right). Line types as in figure 4.

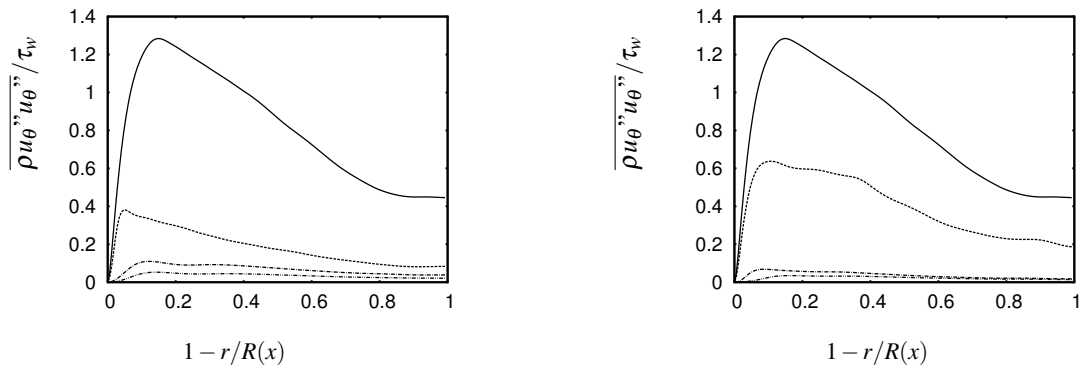


Figure 8. Azimuthal Reynolds stress profiles for case 1 (left) and case 2 (right). Line types as in figure 4.

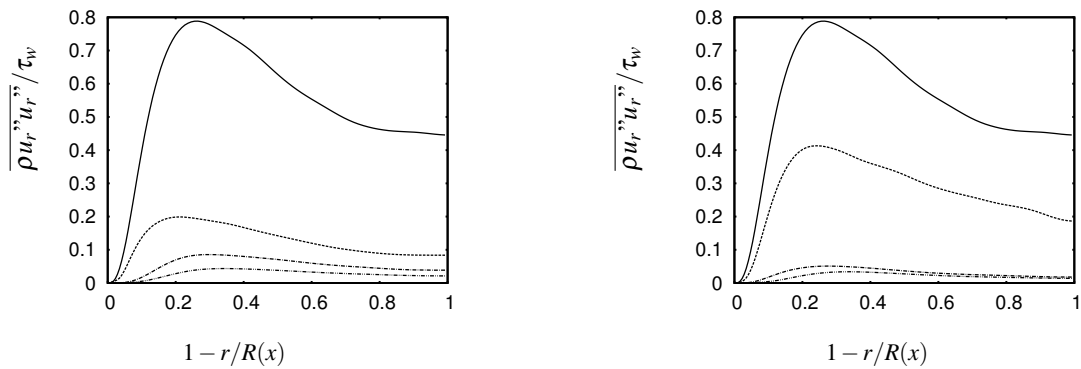


Figure 9. Radial Reynolds stress profiles for case 1 (left) and case 2 (right). Line types as in figure 4.

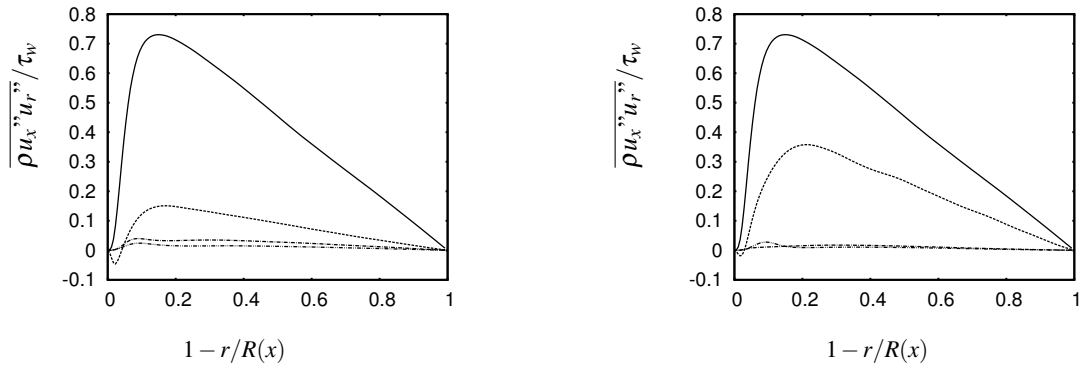


Figure 10. Reynolds shear stress profiles for case 1 (left) and case 2 (right). Line types as in figure 4.

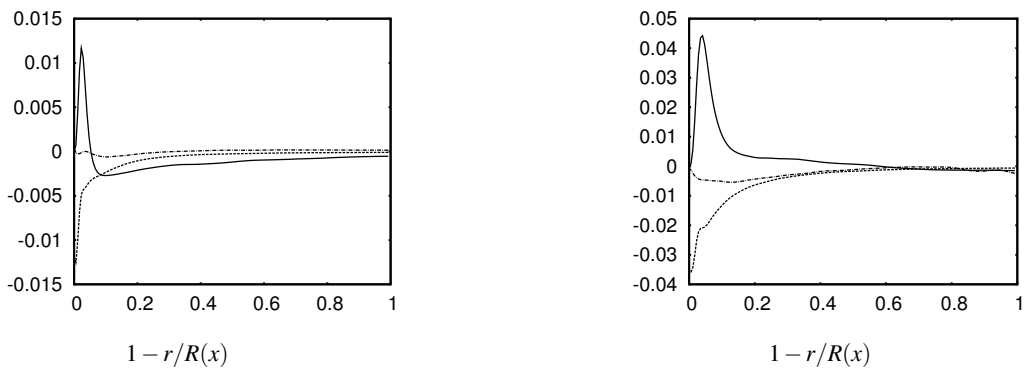


Figure 11. Axial Reynolds budget terms for case 1 (left) and case 2 (right) in the converging portion at $x/L = 0.25$. Solid line: Production, dashed line: dissipation, dashed-dotted line: pressure-strain.

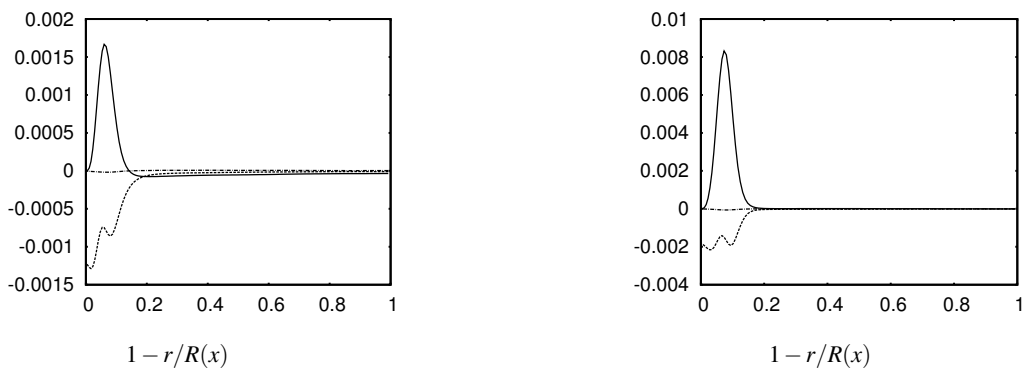


Figure 12. Axial Reynolds budget terms in the divergent portion at $x/L = 0.8$. Case 1 (left), Case 2 (right). Solid line: Production, dashed line: dissipation, dashed-dotted line: pressure-strain.